DRAFT VERSION NOVEMBER 16, 2018
Preprint typeset using LaTeX style emulateapj v. 12/16/11

COMPREHENSIVE ANALYSIS OF HD 105, A YOUNG SOLAR SYSTEM ANALOG

J. P. MARSHALL[1]
Academia Sinica Institute of Astronomy and Astrophysics, 11F of AS/NTU Astronomy-Mathematics Building, No.1, Sect. 4, Roosevelt Rd, Taipei 10617, Taiwan, R.O.C.

J. MILLI
European Southern Observatory (ESO), Alonso de Córdova 3107, Vitacura, Casilla 19001, Santiago, Chile

É. CHOQUET[2,3]
Department of Astronomy, California Institute of Technology, 1200 E. California Blvd, MC 249-17, Pasadena, CA 91125

C. DEL BURGO
Instituto Nacional de Astrofísica, Óptica y Electrónica, Luis Enrique Erro 1, Sta. Ma. Tonantzintla, Puebla, Mexico

G. M. KENNEDY
Department of Physics, University of Warwick, Coventry CV4 7AL, UK

L. MATRÀ
Harvard-Smithsonian Center for Astrophysics, 60 Garden Street, Cambridge, MA 02138, USA

S. ERTEL
Steward Observatory, University of Arizona, 933 N Cherry Ave, Tucson, AZ 85719, USA

A. BOCCALETTI
LESIA, Observatoire de Paris, PSL Research University, CNRS, Sorbonne Universités, UPMC Univ. Paris 06, Univ. Paris Diderot, Sorbonne Paris Cité
Draft version November 16, 2018

ABSTRACT

HD 105 is a nearby, pre-main sequence G0 star hosting a moderately bright debris disc ($L_{\rm dust}/L_\star \sim 2.6 \times 10^{-4}$). HD 105 and its surroundings might therefore be considered an analogue of the young Solar System. We refine the stellar parameters based on an improved Gaia parallax distance, identify it as a pre-main sequence star with an age of 50 $\pm$ 16 Myr. The circumstellar disc was marginally resolved by *Herschel*/PACS imaging at far-infrared wavelengths. Here we present an archival ALMA observation at 1.3 mm, revealing the extent and orientation of the disc. We also present *HST*/NICMOS and VLT/SPHERE near-infrared images, where we recover the disc in scattered light at the ≥ 5-σ level. This was achieved by employing a novel annular averaging technique, and is the first time this has been achieved for a disc in scattered light. Simultaneous modelling of the available photometry, disc architecture, and detection in scattered light allow better determination of the disc's architecture, and dust grain minimum size, composition, and albedo. We measure the dust albedo to lie between 0.19 and 0.06, the lower value being consistent with Edgeworth-Kuiper belt objects.

Keywords: stars: circumstellar matter – stars: planetary systems – stars:individual (HD 105)

1. INTRODUCTION

Through the results of the *Kepler* transit-based exoplanet survey, we are now aware that exoplanets are near-ubiquitous (Coughlin et al. 2016; Foreman-Mackey et al. 2016). Circumstellar debris, most commonly identified through excess emission at infrared wavelengths (Matthews et al. 2014), is less frequently found. However, this is more severely biased and limited by current instrumental sensitivity. A detection rate of 20 % has been recorded for cool discs around nearby FGK-type stars (Eiroa et al. 2013; Montesinos et al. 2016), with a slightly higher detection rate around A-type stars (Thureau et al. 2014). A tentative trend for a higher incidence of debris discs is seen around stars with sub-Solar metallicities hosting low mass planets (Wyatt et al. 2012; Marshall et al. 2014a). For high mass planets, a recent study of disc-host systems has identified a tentative correlation between the presence of $> 5\ M_{\rm Jup}$ planets and debris discs (Meshkat et al. 2017). A study of exoplanet host stars and debris discs reveals a trend between these components of planetary systems being seen together (Matthews et al. 2014). However, no evidence of correlations between these properties has been seen in larger stellar samples, whilst potentially attributable to the paucity

[1] Computational Engineering and Science Research Centre, University of Southern Queensland, Toowoomba, QLD 4350, Australia
[2] Jet Propulsion Laboratory, California Institute of Technology, 4800 Oak Grove Drive, Pasadena, CA 91109, USA
[3] *Hubble* Fellow

of information on both faint debris discs and low mass planets around nearby stars, the presence of real correlations cannot be ruled out due to sample construction (Moro-Martín et al. 2015).

A critical component in developing an understanding of the diversity of architectures exhibited by known planetary systems is to obtain multi-wavelength resolved images of their dusty debris discs (e.g. Ertel et al. 2014; Marshall et al. 2014b, 2016; Hengst et al. 2017). Using a sample of 34 resolved debris discs a relationship between stellar luminosity and dust properties has been identified, showing that the dust grains around higher luminosity stars are closer to emitting like blackbodies (Pawellek et al. 2014). Fitting that observed relationship with a range of dust material compositions further identified that a mixture of astronomical silicate and water ice provided the best fit to the distribution of spatially resolved discs (Pawellek & Krivov 2015). The presence of icy material in cool debris discs has also been inferred through modelling of continuum emission of several spatially resolved debris discs, supporting the adoption of icy materials in the analysis of debris dust (Lebreton et al. 2012; Morales et al. 2016). More recently, a relationship between stellar luminosity and disc radius has been measured for a similar sized sample of debris discs imaged at sub-millimetre wavelengths (Matrà et al. 2018a). However, no evidence was found for the trend of disc radius relative to blackbody radius identified at far-infrared wavelengths. This may be attributed to the low spatial resolution and bias toward higher luminosity stars of the far-infrared sample making it less representative overall.

Analysis of the infrared continuum emission from debris dust can only take our understanding so far. To obtain insight into the dust grain composition and structure (porosity) we require measurement of the silicate features at mid-infrared wavelengths (e.g. Beichman et al. 2006; Chen et al. 2006; Lawler et al. 2009; Johnson et al. 2012; Mittal et al. 2015), and/or measurement of scattered light from the disc (either total intensity or polarised light). A review of recent advancements in the interpretation of scattered light imaging of debris discs is presented in Hughes et al. (2018). In the case of silicate features, a minority of debris disc host stars exhibit features in their mid-infrared spectra (Beichman et al. 2006; Chen et al. 2014), suggesting the constituent dust grains are large ($>$ 10 μm) and/or cold. In the latter case, the scattered light brightness is poorly correlated with expectations from the disc brightness in continuum emission (e.g. Schneider et al. 2014) but, for those discs that have been imaged in scattered light, determination of the dust optical and scattering properties has been possible (e.g. Graham et al. 2007; Krist et al. 2010; Rodigas et al. 2012, 2014; Soummer et al. 2014; Choquet et al. 2016; Schneider et al. 2016). Complementary to the properties of solid material in debris discs, the recent detections of a gaseous component to some of these systems (Greaves et al. 2016) provides insight into the volatile content of the dust parent bodies (e.g. Matrà et al. 2017), and its origins (Kral et al. 2017).

For Sun-like stars, from which we may draw parallels with the evolution of the Solar System, there exist only a few cases with comprehensive multi-wavelength data sets to support such detailed analyses, e.g. HD 15115 (Debes et al. 2008; MacGregor et al. 2015), HD 61005 (Hines et al. 2007; Maness et al. 2009; Buenzli et al. 2010; Olofsson et al. 2016), HD 107146 (Ertel et al. 2011; Ricci et al. 2015; Marino et al. 2018), HD 207129 (Krist et al. 2010; Marshall et al. 2011; Löhne et al. 2012), HIP 17439 (Ertel et al. 2014; Schüppler et al. 2014), and HD 10647 (Liseau et al. 2010; Schüppler et al. 2016). The addition of more targets to this list, particularly within the narrow range of stellar spectral types representative of Solar analogues (i.e. early G-type main sequence stars cf a broad range of F6 to K0 spectral types), is therefore important to understand the diversity of potential outcomes for planet formation processes. The relative novelty of the Solar System may therefore be determined by comparison to the range of properties exhibited by analogous debris discs systems.

HD 105 is a young, Sun-like star at a distance of 40 pc that hosts a moderately bright debris disc ($L_{\rm dust}/L_{\star} \sim 2.6 \times 10^{-4}$). HD 105 is a member of the Tucana-Horologium association and has a well established age of 28 $\pm$ 4 Myr (Torres et al. 2000; Zuckerman & Webb 2000). Its debris disc was reported as being marginally resolved in far-infrared *Herschel*/PACS imaging observations and found to have a radius of $\sim$ 50 au (Donaldson et al. 2012). With a spectral type of G0, HD 105 might therefore be considered an analogue of the young Solar System.

Here we model the continuum emission and structure of HD 105's debris disc using a combination of far-infrared and sub-millimetre photometry obtained from a new reduction of archival *Herschel*/PACS and SPIRE images, and a spatially resolved archival image of the disc at millimetre wavelengths from ALMA. We complement this approach with analysis of near-infrared images from *HST*/NICMOS and VLT/SPHERE in order to constrain the dust optical properties through scattered light.

In Sect. 2, we present the imaging and photometric data compiled to model both the stellar and disc components of this system. In Sect. 3 we lay out our approach to analysing the combined data set and state our findings. Sect. 4 the results are put in context, and their impact on our understanding of this system. Finally, in Sect. 5, we summarise our findings and detail the conclusions of this work.

2. OBSERVATIONS

We have compiled broad band photometric data from optical to millimetre wavelengths to construct the SED of HD 105. These previous observations, combined with the ALMA, VLT/SPHERE, and *HST*/NICMOS imaging data presented here, facilitate comprehensive modelling of the HD 105 system. A summary of the photometry used in the modelling process is presented in Table 1.

At optical wavelengths we use the Strömgren data from Paunzen (2015), Johnson *BV* and Cousins *I* data from (Mermilliod et al. 1997), near-infrared 2MASS JHK_s (Cutri et al. 2003), and *WISE* W1 and W2 fluxes (Wright et al. 2010) to scale the model stellar photosphere and gauge its contribution to the total emission.

In the mid-infrared, the *WISE* W3 (12 μm) and W4 (22 μm) fluxes are complemented by *AKARI*/IRC 9 μm data point (Ishihara et al. 2010), a *Spitzer*/MIPS measurement at 24 μm, and *Spitzer*/IRS photometry at 13 μm and 31 μm. The *Spitzer*/IRS spectrum was obtained from CASSIS[4] (Lebouteiller et al. 2011). As the target exhibits no evidence of mid-infrared excess, the spectrum was scaled to the photospheric model using a least-squares fit weighted by the measurement uncertainties at wavelengths $<$ 15 μm. Target fluxes were then extracted in two windows centred at 13 and

[4] The Cornell Atlas of Spitzer/IRS Sources (CASSIS) is a product of the Infrared Science Center at Cornell University, supported by NASA and JPL.

31 μm and 4 μm in width using the error-weighted average of values within the bin.

At far-infrared wavelengths, we combine *ISO*/ISOPHOT measurements at 60 and 90 μm (Spangler et al. 2001) and a *Spitzer*/MIPS measurement at 70 μm (Carpenter et al. 2009) with *Herschel*/PACS measurements at 70, 100, and 160 μm. The spatial resolution of *ISO* is much poorer (1.5′ beam FWHM) than *Spitzer* or *Herschel* (6–18″ beam FWHM); inclusion of background contamination and errors in the zero level calibration elevating the *ISO*-measured fluxes are possibilities (Héraudeau et al. 2003; del Burgo et al. 2003). However, the target is well isolated in the *Herschel* maps and there is good agreement between measurements by all three facilities at similar wavelengths so we therefore do not consider it to have a significant impact on the shape of the SED.

The *Herschel*[5] observations were first presented in Donaldson et al. (2012). Here we re-reduced these data to obtain revised values for the source fluxes based on updates to the instrument calibration made available in the intervening time. The data reduction and analysis were carried out in the same manner as described in Eiroa et al. (2013). The PACS data were reduced in the *Herschel* Interactive Processing Environment[6] (HIPE, Ott 2010) using the standard pipeline processing scripts (HIPE version 15, PACS calibration 78). Target fluxes were measured in each mosaic using an aperture of 15″radius and a sky annulus of 30 to 40″. Appropriate aperture and colour corrections (determined by a blackbody fit to the aperture corrected measurements), based on values tabulated in Balog et al. (2014), were applied to the measurements before modelling.

We also present sub-millimetre measurements taken from *Herschel*/SPIRE (Programme ot2_aroberge_3, PI: A. Roberge) and an APEX/LABOCA measurement at 880 μm (Nilsson et al. 2010). The SPIRE observations were again reduced in HIPE version 15, using SPIRE calibration 14_3. The target fluxes in the three SPIRE maps were measured using the *sourceExtractorSussextractor* routine. The millimetre SED is further constrained by ALMA photometry at 1300 μm (Programme 2012.1.00437.S, PI: D. Rodriguez) and an ATCA measurement at 9 mm taken from Marshall et al. (2017).

3. METHODOLOGY AND RESULTS

Here we undertake a determination of the stellar parameters by fitting a grid of stellar atmosphere models to archival high resolution spectra. We also inferred the same stellar parameters as well as the mass and age from stellar evolution models combined with a Bayesian approach. We then present a self-consistent analysis of both the millimetre and scattered light imaging data to determine the disc architecture and dust albedo, respectively. The disc structure is applied as a constraint in modelling of the disc spectral energy distribution (SED) in combination with photometry from archival sources.

3.1. *Stellar parameters*

A summary of the stellar properties used in this work are given in Table 2. The stellar position, distance (parallax), proper motions, and G band magnitude ($G = 7.3833 \pm 0.0007$) are taken from the Gaia DR 2 catalogue (Gaia Collaboration et al. 2016; Lindegren et al. 2016; Gaia Collaboration et al. 2018). The stellar physical properties were derived by modelling of available high resolution spectra along with optical and near-infrared photometry.

[5] *Herschel* is an ESA space observatory with science instruments provided by European-led Principal Investigator consortia and with important participation from NASA.

[6] HIPE is a joint development by the Herschel Science Ground Segment Consortium, consisting of ESA, the NASA Herschel Science Center, and the HIFI, PACS and SPIRE consortia.

Table 1
Photometry used in disc modelling.

Wavelength (μm)	Flux (mJy)	Instrument/ Filter	Ref.
0.349	891 ± 2	Strömgren *u*	1
0.411	2071 ± 6	Strömgren *b*	1
0.440	1897 ± 14	Johnson *B*	2
0.467	2989 ± 6	Strömgren *v*	1
0.546	3669 ± 2	Strömgren *y*	1
0.550	3499 ± 26	Johnson *V*	2
0.790	4468 ± 41	Cousins *I*	3
1.235	4139 ± 73	2MASS *J*	4
1.662	3425 ± 73	2MASS *H*	4
2.159	2383 ± 42	2MASS K_s	4
3.40	1152 ± 122	*WISE* W1	5
4.60	699 ± 24	*WISE* W2	5
9.00	189 ± 13	AKARI/IRC9	6
12.0	114 ± 6	*WISE* W3	5
22.0	35 ± 2	*WISE* W4	5
24.0	29 ± 1	*Spitzer*/MIPS	7
31.0	22 ± 7	*Spitzer*/IRS	8
60.0	143 ± 3	*ISO*/PHT	9
70.0	141 ± 10	*Spitzer*/MIPS	7
70.0	132 ± 8	*Herschel*/PACS	10
90.0	167 ± 8	*ISO*/PHT	9
100.0	168 ± 8	*Herschel*/PACS	10
160.0	112 ± 9	*Herschel*/PACS	10
250.0	57 ± 10	*Herschel*/SPIRE	11
350.0	38 ± 15	*Herschel*/SPIRE	11
880.0	10.7 ± 5.9	APEX/LABOCA	12
1300.0	2.0 ± 0.4	ALMA	11
9000.0	0.042 ± 0.014	ATCA	13

References. — 1. Paunzen (2015); 2. Mermilliod et al. (1997); 3. Perryman et al. (1997); 4. Cutri et al. (2003); 5. Wright et al. (2010); 6. Ishihara et al. (2010); 7. Carpenter et al. (2009); 8. Chen et al. (2014); 9. Spangler et al. (2001); 10. Donaldson et al. (2012); 11. This work; 12. Nilsson et al. (2010); 13. Marshall et al. (2017).

Table 2
Summary of stellar parameters.

Parameter	Value	Ref.
Right Ascension (*hms*)	00 05 52.54	1
Declination (*dms*)	-41 45 11.0	1
Proper motions (mas/yr)	97.96, -76.51	2
Distance (pc)	38.85 ± 0.08	2
V (mag)	7.513 ± 0.005	3
$B-V$ (mag)	0.600 ± 0.003	3
Spectral type	G0	4
Luminosity ($L_\odot$)	1.216 ± 0.005	4
Radius ($R_\odot$)	1.009 ± 0.003	4
Mass ($M_\odot$)	1.116 ± 0.012	4
Temperature (K)	6034 ± 8	4
Surface gravity, $\log g$	4.478 ± 0.006	4
Metallicity, [Fe/H]	0.02 ± 0.04	5
$\nu \sin i$ (km/s)	17.5 ± 0.5	4
Age (Myr)	50 ± 16	4

References. — 1. van Leeuwen (2007); 2. Lindegren et al. (2016); Gaia Collaboration et al. (2016, 2018); 3. Mermilliod et al. (1997); 4. This work; 5. Tsantaki et al. (2014)

The stellar parameters of HD 105, i.e. luminosity, radius, effective temperature, surface gravity, age, and mass, were derived by using the absolute G magnitude, parallax, $B-V$ colour, and [Fe/H] as input parameters using the Bayesian approach applied in del Burgo & Allende Prieto (2016, 2018). We derived an age of 50 $\pm$ 16 Myr, which is in agreement with that one more constrained assuming membership of Tucana Horologium, of 30 Myr (del Burgo et al. in preparation). The colour $B-V = 0.600 \pm 0.003$ is taken from Mermilliod et al. (1997), and metallicity [Fe/H] = 0.02 $\pm$ 0.04 from Tsantaki et al. (2014). The observed G magnitude was converted to absolute magnitude M_G using the *Gaia* DR2 parallax of $\pi = 25.75 \pm 0.06$ mas (Gaia Collaboration et al. 2018). We find that HD 105 is a pre-main-sequence star. In order to derive the stellar parameters we downloaded and arranged a grid of PARSEC isochrones (version 1.2S, Bressan et al. 2012; Chen et al. 2014, 2015; Tang et al. 2014), with steps in age of 5 per cent, steps in mass of 0.1 per cent, and steps of 0.02 dex in [Fe/H]. The lower and upper limits of these parameters are well beyond 6-σ around the solution, see Table 2. Synthetic photometry estimates were obtained using filter curves from Evans et al. (2018) for the Gaia G band, and Maíz Apellániz (2006) for the B and V bands. For a more detailed description see del Burgo & Allende Prieto (2018).

In addition, high resolution FEROS and HARPS spectra were also used to obtain the stellar effective temperature $T_{\rm eff}$, metallicity [Fe/H], projected rotational velocity $\nu \sin i$, and surface gravity $\log g$. We performed a comparison with BT-Settl stellar atmosphere models (Allard et al. 2012). The models in the grid were modified in order to be compared with the FEROS spectrum similar to the approach of del Burgo et al. (2009). First, the synthetic spectra were transformed to take into account the stellar projected rotational velocity ($\nu \sin i$) using the formalism of Gray (1992), with a limb darkening parameter equal to 0.8. These spectra were convolved with a Gaussian that mimics the instrumental profile along the dispersion axis. The resulting spectra were rebinned to the same resolution and grid of the observed spectrum. This was corrected from the velocity shift from a cross-correlation analysis with the models. All modelled and observed spectra were normalized before performing the comparison.

We obtain values from the FEROS spectrum ($R = 48,000$) of $T_{\rm eff} = 6000 \pm 50$ K, $\log g = 4.50 \pm 0.25$, and $\nu \sin i = 17.5 \pm 0.5$ km/s. Values derived from the higher resolution HARPS spectrum ($R = 115,000$) are consistent with those of FEROS, with the FEROS values being determined at higher signal-to-noise. These values are consistent with those derived from the aforementioned stellar atmosphere models.

We have a good agreement between the stellar evolution analysis and the stellar atmosphere model fitting for the parameters in common. The values obtained through this analysis are likewise consistent with available values from the literature e.g. Valenti & Fischer (2005), Tsantaki et al. (2014).

The Hα and CaII H&K lines in the FEROS spectrum are presented in Fig. 1. The median FEROS spectrum, calculated from the available spectra (in black) is plotted together with our best fitting model. Some regions of the Hα segment of the spectrum have been blanked out due to contamination from telluric lines at those wavelengths (see Fig. 1, top). Despite the low $\nu \sin i$ (consistent with a more pole-on viewing angle), we see clear evidence of CaII H&K emission in the spectrum (see Fig. 1, bottom). This is consistent with activity in the stellar chromosphere, an indicator of stellar youth.

We also examined the high resolution spectra for evidence of gas revealed by the presence of circumstellar absorption or emission lines. The origin of such gas may be primordial, or secondary from e.g. photodesorption or cometary activity. We note that the FEROS fibre input has a 2″ footprint on the sky that could include light scattered from material in the circumstellar disc, depending on the seeing quality. No evidence of such features is seen. No evidence of gas features in either absorption (implying cool gas) or emission (implying hot gas) were identified in the spectra.

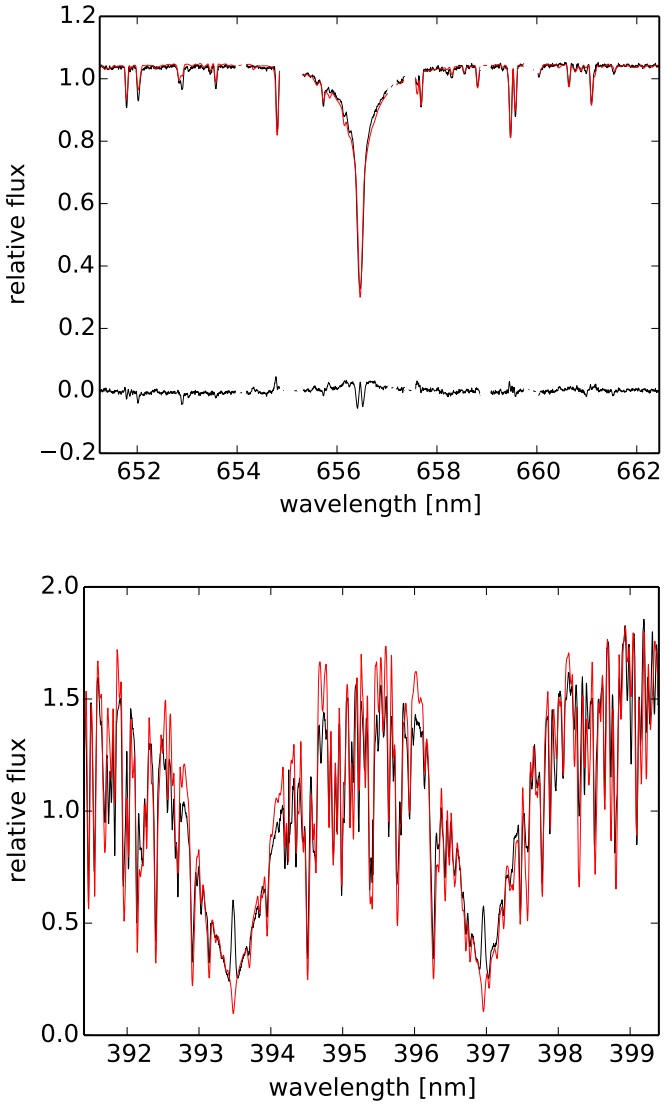

Figure 1. Segments of the FEROS spectrum covering the Hα (top) and CaII H&K (bottom). The median stellar spectrum from X FEROS observations is presented in black, whilst the best-fitting model is presented in red. Some regions have been blanked out due to contamination from telluric lines. The residual (observed-model) spectrum is shown for clarity in the Hα panel.

3.2. *ALMA millimetre imaging data*

An ALMA band 6 (1.3 mm) observation for HD 105 was downloaded from the ESO ALMA Science Archive[7]. The observation was originally carried out as part of project 2012.1.00437.S (PI: D. Rodriguez) during Cycle 1. The spectral setup consists of four windows. Three windows were set

[7] http://almascience.eso.org/aq/

Table 3
Architecture of HD 105's disc determined from the ALMA image.

Parameter	Range	Values	Spacing	Value
Inclination (°)	0 – 90	19	Linear	50 ± 5
Position Angle (°)	0 – 90	19	Linear	15 ± 5
Semi-major axis (au)	50 – 150	41	Linear	85 ± 5
Semi-major axis ($''$)				2.16 ± 0.13
Belt width (au)	10 – 50	21	Linear	30 ± 10
Belt width ($''$)				0.75 ± 0.25
S.B. exponent, α	0.0	1	Fixed	0.0
Total disc flux (mJy)	1.0 – 4.0	301	Linear	1.45 ± 0.28
Dust mass ($M_\oplus$)				$0.035^{+0.013}_{-0.009}$

up to measure the continuum, each with 128 channels over 2 GHz bandwidth. The fourth covered the ^{12}CO (2-1) line at 230.538 GHz and sampled its 0.94 GHz bandwith with 3840 channels (0.32 kms^{-1}), providing a velocity resolution of 0.64 kms^{-1}. In combination, the four channels provide 6.9 GHz bandwidth to study the continuum emission. The on-source integration time for HD 105 was 2238 s. Neptune was used as the flux calibrator, J0006-0623 was the bandpass calibrator, and J0012-3954 was the phase calibrator.

Calibration and reduction of the ALMA observation were carried out in CASA 4.1 using the provided scripts. Image reconstruction was carried out using the *clean* task combining all four spectral windows for the greatest signal-to-noise. We reconstruct the image using natural weighting. With natural weighting the continuum image r.m.s. noise is 26.8 μJy beam^{-1}. The dirty beam has an ellipsoidal FWHM $0.''95 \times 0.''67$ at a position angle of 88°, equivalent to a spatial resolution of 34 × 26 au.

3.2.1. *Disc architecture*

The disc is visible as an annular structure centred on the stellar position, but the low signal-to-noise of the observations means that it is not detected with high significance ($> 3-\sigma$) at all position angles. The ALMA image and the best fit annular disc model are presented in Fig. 2.

We model the architecture of HD 105's disc as a single annulus with a semi-major axis R and width ΔR oriented at a position angle θ and inclination i. The disc surface brightness exponent α is assumed to be constant, and a vertical opening angle of 10°, similar to the Solar system, was assumed. A grid of models is generated spanning reasonable values for each of these parameters. To determine the best-fit properties for the disc we subtract each disc model, convolved with the dirty ALMA beam (FWHM $\sim 0.''9 \times 0.''7$), from the observed image and seek to minimise the residuals within the region of the model-subtracted image where there is significant emission in the observed image.

The best-fit architecture derived from the model fitting is dominated by the disc ansae, which are the only regions of the disc detected at high signal-to-noise (> 3-σ). The disc semi-major axis is $2.''16 \pm 0.''13$ (85 ± 5 au), with an inclination of 50 ± 5 °with respect to the line of sight at a position angle of 15 ± 5°. The width of the disc annulus is $0.''75 \pm 0.''25$ (30 ± 10 au). The belt is perhaps marginally resolved in the ALMA image, but the quality of the data does not allow us to conclude that, so we hereafter assume the belt is unresolved. The best-fit disc architecture obtained from this approach is summarised in Table 3.

The total flux of the disc in the sub-millimetre, 1.45 ± 0.28 mJy, may be used to calculate the mass of dust grains, assuming that the disc is fully optically thin at 1.3 mm. For a disc observed at a frequency ν with a flux F_ν the dust mass, $M_{\rm dust}$, is given by

$$M_{\rm dust} = F_\nu d_\star^2 / \kappa_\nu B_{\nu, T_{\rm dust}} \quad (1)$$

where $d_\star$ is the stellar distance, κ_ν is the dust opacity, $T_{\rm dust}$ is the dust temperature, and $B_{\nu,T_{\rm dust}}$ is the Planck function (Zuckerman & Becklin 1993; Draine 2006). Assuming the dust opacity κ is 1.7 gcm^{-2} (Beckwith et al. 1990; Pollack et al. 1994; Draine 2006), that is commonly assumed for debris dust (e.g. Panić et al. 2013; Holland et al. 2017), we calculate a mass of $0.035^{+0.013}_{-0.009}$ M$_\oplus$ for the dust. This value does not include uncertainty on the parameter κ, which leads to an uncertainty in $M_{\rm dust}$ of a factor 3 to 5.

3.2.2. *Non-detection of cold CO emission*

Molecular carbon monoxide (CO) has been identified in around a dozen debris disc systems (e.g. Greaves et al. 2016; Moór et al. 2017), believed in most cases to be the result of secondary production after liberation from exocomets (Kral et al. 2017). Most of the stars identified with gas in their debris discs are young ($t_{\rm age} < 30$ Myr) A-type stars, with relatively bright debris discs ($L_d/L_\star \sim 10^{-3}$). Here we search the ALMA observation for emission from the disc associated with the CO (2-1) transition at 230.538 GHz following the method employed to extract CO emission at low signal-to-noise in ALMA data as presented in Matrà et al. (2015); Marino et al. (2016, 2017).

To begin we produced a continuum subtracted measurement set from the HD 105 data using *uvcontsub*. The continuum subtracted data set is then *clean*ed to produce an image cube with the same weighting and pixel scale as the continuum image. The cube spans barycentric velocities between -25 and 25 kms^{-1}, with a step size of 0.5 kms^{-1}. The cube is corrected for the effect of the primary beam using the *impbcor* task before further analysis. No significant CO emission is observed in the velocity-integrated, continuum-subtracted image produced by integrating the cube.

We then proceed by implementing the spectro-spatial filtering technique presented in Matrà et al. (2017). Any circumstellar CO is assumed to originate from collisions between planetesimals and therefore reside in the same region around the star as the debris dust detected in the continuum image. The CO is further assumed to be situated in a vertically flat disc, orbiting with Keplerian velocity around a star of 1.114 $M_\odot$. We then determine the projected radial velocity for each position in the disc image given the extent and inclination of the disc for cases of the disc rotating toward or away from us. Using the predicted velocity field the spectrum at each position is then shifted to match the stellar velocity (i.e. spectral filtering). We then integrate over all positions where continuum emission is detected to avoid contributions to the CO spectrum from locations and velocities where no circumstellar CO is expected (i.e. spatial filtering). The spectro-spatial filtering yields a 3-σ upper limit of 8.5 mJy kms^{-1} to CO emission.

We use a non-Local Thermodynamic Equilibrium CO excitation code to calculate a CO mass upper limit, following Matrà et al. (2018b). This code includes fluorescent excitation from the central star at ultraviolet wavelengths. Depending on the excitation conditions we determine a CO mass upper limit ranging from 2.5×10^{-7} to 2.5×10^{-6} $M_\oplus$. This translates

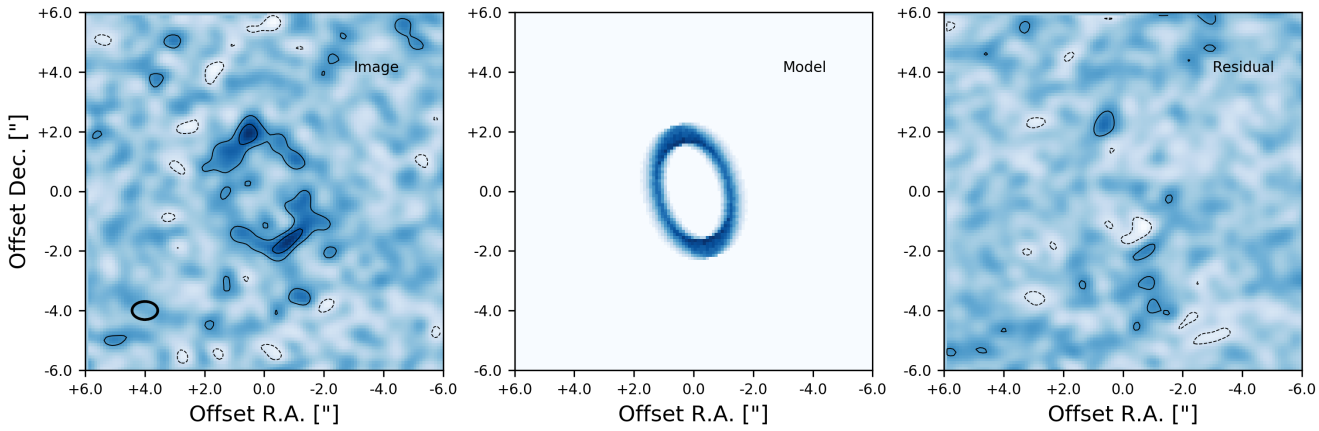

Figure 2. ALMA 1.3 mm (Band 6) naturally weighted, dirty image of HD 105, the best fit annular model for the disc, and the residuals in the observed image after subtraction of a model convolved with the dirty beam (from left to right). Orientation is north up, east left. The colour scale for the observations and residuals is linear between -3-σ and +3-σ. The ALMA beam is represented by the black ellipse in the bottom left of the observation. Contours are at -2, 2, 4, and 6-σ, with the broken contour denoting negative values.

to upper limits on the CO and CO_2 fraction (by mass) in exocomets between $<$ 88 % and $<$ 46 % for the respective mass upper limits. This limit is consistent with the range of values for other exocometary discs, and Solar system bodies (see e.g. Matrà et al. 2017).

3.3. *Detection of scattered light*

HD 105 has been observed by both *HST*/NICMOS and VLT/SPHERE. The disc was not directly visible in either data set. However, we recover the disc at the correct angular separation and orientation using an angular averaging technique to aggregate the disc emission to a detectable level. From this measurement of the disc scattered light brightness we determine the albedo of the dust grains at near-infrared wavelengths.

3.3.1. *HST/NICMOS*

HD 105 was observed with the *Hubble Space Telescope* (HST) NICMOS instrument at two epochs using the coronagraphic mode (mask radius 0.″3) of the mid-resolution NIC2 channel (0.″07565 pixel^{-1}). The first data were acquired on UT-1998-11-03 as part of program GTO-7226 (PI: E. Becklin), a survey looking for giant planets around young nearby stars (Lowrance et al. 2005), using the F160W filter of bandpass very comparable to the H band (pivot wavelength 1.600 μm, 98%-integrated bandwidth 0.410 μm). The second dataset was obtained on UT-2006-07-23 as part of program GO-10527 (PI: D. Hines), a survey looking for debris discs around stars with infrared excess detected with *Spitzer* as part of the FEPS program (Hillenbrand et al. 2008). The data were obtained with the F110W filter, which is twice as extended toward shorter wavelengths as the J band (pivot wavelength 1.116 μm, 98%-integrated bandwidth 0.584 μm).

The F160W data were acquired at two different spacecraft orientations, obtaining a total of 6 exposures with HST rolled by $\sim$ 30° in the middle of the sequence, to enable subtraction of the PSF with Roll Differential Imaging (Lowrance et al. 1999). The total exposure time is 1344 s for this dataset. The F110W dataset includes 7 exposures all obtained with the same telescope orientation, for a total exposure time of 2016 s.

We reprocessed both datasets as part of the *Archival Legacy Investigations for Circumstellar Environments* (ALICE) program (PI: R. Soummer), a consistent re-analysis of the NICMOS coronagraphic archive using modern PSF subtraction techniques (Choquet et al. 2014; Hagan et al. 2018). Assembling PSF libraries from multiple reference stars in the whole archive and using the PCA-based KLIP algorithm for PSF subtraction (Soummer et al. 2012), this program demonstrated a gain in point source sensitivity by a factor of 20 at 1″ from the star over classical reference star differential imaging (Debes et al. 2016), and enabled the detection of 11 faint debris discs from NICMOS archival data (Soummer et al. 2014; Choquet et al. 2016, 2017, 2018).

For HD 105, we used the reprocessed data from the ALICE public database[8] for the F110W dataset, and an unpublished ALICE reduction for the F160W dataset with an $11 \times 11''$ field of view, more favorable to disc detection with sensitivity limits better than the data published in the ALICE database. PSF subtraction for the F160W dataset was achieved using the 69 first eigen-modes of a library assembling 125 images from reference stars exclusively, and excluded a central zone within a radius of 12 pixels. The F110W dataset was PSF-subtracted with the 211 first eigen-modes of a 640-image library from reference stars only, excluding a central area of radius 5 pixels. The final images were obtained by rotating all exposures to North pointing up, co-adding and scaling them to surface brightness units based on NIC2's plate-scale and its calibrated photometric factors (F_ν = 1.21121 μJy s DN^{-1} in F110W, F_ν = 1.49585 μJy s DN^{-1} in F160W). We are able to recover the disc scattered light in the F160W filter image in the disc's ansae at low signal-to-noise, as shown in Fig. 3.

To obtain a more significant measurement of the disc surface brightness than can be obtained from the reduced images, we make use of the high spatial resolution of the scattered light image and measure the surface brightness radial profiles. We computed the surface brightness averaged in

[8] https://archive.stsci.edu/prepds/alice/

5-pixel wide (0.38″) elliptical apertures of increasing semi-major axes a with semi major axis a increasing with steps of 1 pixel (76 mas) and semi-minor axis $b = a\cos(50°)$, oriented 15° east-of-north, to trace the disc deprojected average radial profile according to the ALMA detection geometry. We estimate the corresponding uncertainties assuming uncorrelated noise, as $\sigma/\sqrt{(N_{\rm pix})}$ with σ the standard-deviation in each aperture and $N_{\rm pix}$ the number of pixel in the aperture. Since only reference stars were used for PSF subtraction, these measurements are not affected by disc self-subtraction. They are however subject to over-subtraction by the PCA algorithm along with PSF features (Soummer et al. 2012; Pueyo 2016). We corrected our average profiles and uncertainties by estimating the algorithm throughput with analytical forward modeling. From this exercise we find a significant peak with a surface brightness of 15 ± 1 μJy/arcsec^2 at a separation of around 2.2″ from the star, consistent with the ALMA image. The binned radial profiles are presented in Fig. 3.

3.3.2. *VLT/SPHERE*

HD 105 was observed with the Spectro-Polarimeter High-contrast Exoplanet REsearch (SPHERE, Beuzit et al. 2008) on the night of October, 2nd 2015. These observations used the Infra-Red Dual-beam Imager and Spectrograph (IRDIS, Dohlen et al. 2008) of SPHERE to obtain high-contrast and high-angular resolution images of the circumstellar environment of HD 105, in the broad-band H filter (centred at 1.625 μm, width 291 nm) with the apodized Lyot coronagraph of diameter 185mas. They are part of the SPHERE High-Angular Resolution Debris Disc Survey[9] (SHARDDS, Milli et al. in prep.). SHARDDS is an open-time program on SPHERE to perform the first comprehensive near-infrared survey of all bright, nearby debris discs (infrared excess greater than 10^{-4}), yet undetected in scattered light, within 100 pc. It already led to detections of several discs and a brown dwarf companion: HD 114082 (Wahhaj et al. 2016), 49 Ceti (Choquet et al. 2017) and HD 206893 (Milli et al. 2017a). HD 105 was observed for a total of 50 min on-source, among which the total exposure time is 2432 s, in pupil-stabilized mode to allow Angular Differential Imaging (Marois et al. 2006). The source was observed just before meridian crossing, which resulted in a parallactic angle rotation of 35°.

The data were sky-subtracted, flat-fielded and bad pixel corrected using the official SPHERE Data Reduction and Handling pipeline (Pavlov et al. 2008) in order to make a temporal cube of 606 frames. Each coronagraphic frame was re-centred using the set of four satellite spots imprinted in the image during the centring sequence. This sequence is obtained by applying a waffle pattern to the deformable mirror and was done prior to and after the deep science coronagraphic observations. Then, different data reduction techniques were applied to subtract the stellar halo and try to detect the scattered light of the disc.

At the expected semi-major axis of the disc of 2.16″, the technique that yields the best sensitivity for point source detection is the classical Angular Differential Imaging (cADI, Marois et al. 2006) technique. However for an azimuthally extended structure such as the HD 105 disc, the throughput of the algorithm is very low because of self-subtraction (Milli et al. 2012) and we estimated it to be a few percent. The 5-σ sensitivity of the ADI reduction is 100μJy at 2.2″after throughput correction, and we are therefore unable to confirm the *HST*/NICMOS detection with this data reduction technique.

Therefore, we also applied the Reference Star Differential Imaging (R[S]DI) technique, commonly used in space-based observations (Schneider et al. 1999; Lafrenière et al. 2009; Soummer et al. 2011), and more recently applied to ground-based observations (Gerard & Marois 2016). We implemented this technique in the SHARDDS program by building a library of all the coronagraphic images obtained in the program. We then selected 610 images from 22 stars most correlated with the ones from HD 105 (excluding the HD 105 images themselves) and used this set of references to subtract the stellar halo, using a custom PCA algorithm, keeping 100 modes. The disc is not directly visible in the VLT/SPHERE image.

The image is binned by a factor 4, giving a new pixel size of 49 mas, corresponding to the measured FWHM in the non-coronagraphic image. In the image reduced with PCA-RDI, the flux is integrated in elliptical apertures having an aspect ratio matching the inclination of the disc as seen by ALMA, and a radial width of 10 binned pixels or 490 mas. This ellipse is increased iteratively by step of 1 binned pixels or 49 mas, and at each iteration, the signal is computed as the sum of the flux over this elliptical aperture. It is corrected for the PCA throughput and converted in μJy/arcsec^2 using the binned pixel size of 49 mas and the star flux as measured in the non coronagraphic image. The noise is given by the standard deviation of the pixels over the same elliptical annulus.

This averaging technique increases the depth to which we can detect disc scattered light emission using geometrical prior from the resolved mm detection. We find a peak in emission at 5.9 μJy/arcsec^2 for a semi-major axis of 2.3″, consistent with the disc semi-major axis, as shown in Fig. 4. This is a factor of ∼4 fainter than the disc detected by *HST*/NICMOS; examination of the separate channels reveals that the right channel is consistent with the NICMOS-detected signal in both semi-major axis and brightness, but the left channel is not. Both channels are consistent in the presence of emission between 1.5 and 3.5″, consistent with HD 105's disc. The origin of the discrepancy between the *HST*/NICMOS and VLT/SPHERE detections potentially lies in the estimation of noise, which has been assumed Gaussian here, but it can be seen in the reduced image that the noise is non-Gaussian.

3.3.3. *Combined modelling*

The scattered light measurements from *HST*/NICMOS and VLT/SPHERE can be used to calculate the albedo of the dust grains. Assuming optically thin dust, and using the approximation from Weinberger et al. (1999), the maximum allowed optical depth τ times the albedo ω is $4\pi\phi^2 S/F$ where S is the surface brightness of the disc in mJy/arcsec^2, F the total star flux in mJy and ϕ the separation of the scatterers. Approximating the optical depth by $\tau = 2f\phi\cos(i)/[d\phi(1-\omega)]$ where $d\phi$ is the disc width in arcsec and f the fractional luminosity, we obtain:

$$S = \frac{fF\omega}{(2\pi \times \phi \times d\phi \times \cos(i))(1-\omega)} \quad (2)$$

Using a disc semi-major axis $\phi = 2.16''$ with a width $d\phi = 0.75''$ at an inclination $i = 50°$ we obtain an albedo of 0.15 based on the NICMOS surface brightness (15 μJy/arcsec^2),

[9] ESO program ID 096.C-0388(A)

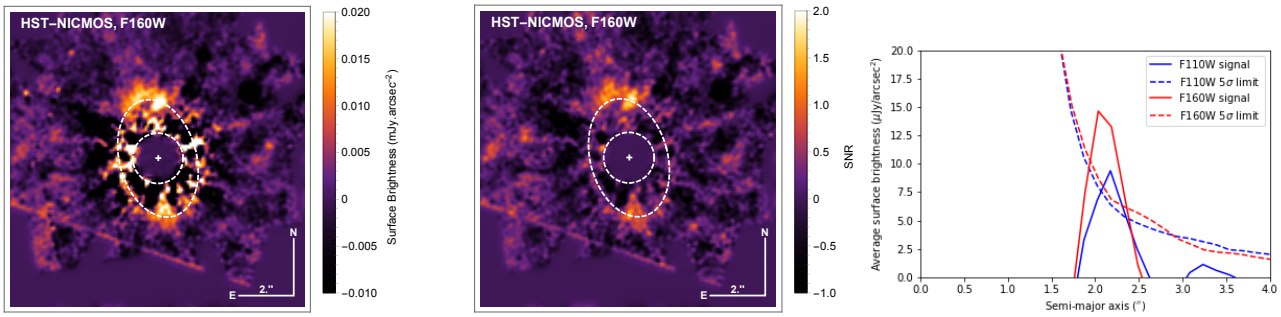

Figure 3. *Left*: *HST*/NICMOS F160W image of HD 105, smoothed by convolution with a model PSF. Significant emission from the disc is recovered at the ansae. The '+' symbol denotes the stellar position, the circular dashed line denotes the numerical mask, and the dashed elliptical line denotes the extent and orientation of the debris disc from the ALMA image. Orientation is north up, east left. *Middle*: Signal-to-noise map of the *HST*/NICMOS image also smoothed by convolution with a model PSF. The noise was estimated from from the pixel-wise standard deviation of reference stars PSF-subtracted with the same parameters as for HD 105 (Choquet et al. 2018). *Right*: Results of elliptical averaging of the *HST*/NICMOS F110W and F160W images, revealing significant emission at the orientation and semi-major axis of HD 105's disc as imaged by ALMA ($i = 50°$, $\theta = 15°$). The signal peaks in the F110W filter around 10μJy/arcsec^2 at a separation of 2.2″, and the signal in the F160W filter peaks at 15μJy/arcsec^2 at a similar separation. The solid blue (red) line denotes the extended emission in F110W (F160W) filter, whilst the dashed red (blue) line denotes the 5-σ surface brightness limit in the respective filters.

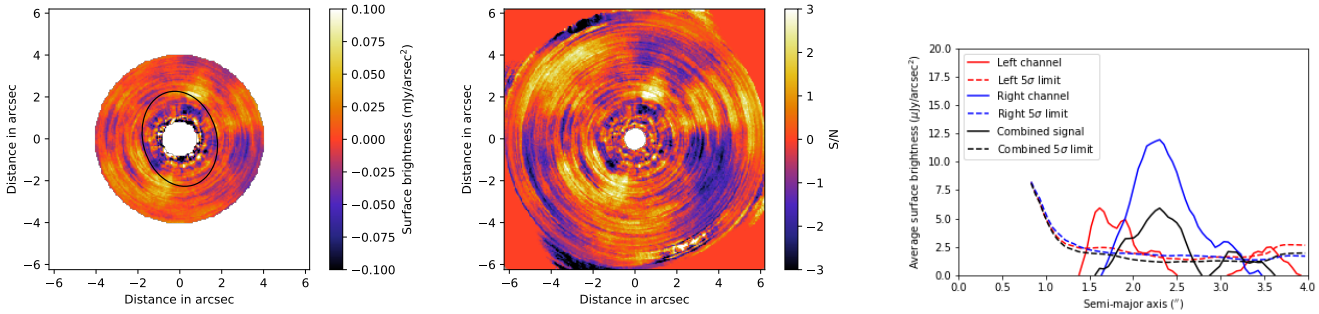

Figure 4. *Left*: VLT/SPHERE PCA-RDI reduced image of HD 105. The black ellipse denotes the location of the disc in the ALMA image. *Middle*: Signal-to-noise map of the VLT/SPHERE image, combining both left and right detector channels. *Right*: Results of elliptical annular averaging of the VLT/SPHERE image, revealing significant emission at the orientation and semi-major axis of HD 105's disc as imaged by ALMA ($i = 50°$, $\theta = 15°$). The emission peaks at 5.9 μJy/arcsec^2 at a separation of 2.3″, denoted by the black solid line in the figure; the black dashed line denotes the 5-σ surface brightness limit. The red and blue lines denote the measured brightness and 5-σ limits for the left and right channels, respectively. We note that the two channels are very different, but are consistent in they reveal significant emission between 1.5 to 3.0″ from the star on the same orientation as the disc in the ALMA image. See text for details.

or 0.06 based on the SPHERE measurement (5.9 μJy/arcsec^2). The apparent surface brightness can be significantly enhanced in case of strong forward scattering (Hedman & Stark 2015; Milli et al. 2017b; Olofsson et al. 2016) but given the inclination of the HD 105 disc scattering angles below 40° are not probed.

With the radial averaging, we have been able to measure dust albedoes a factor of 3 to 10 deeper than expected. The detection of HD 105 in scattered light made here points the way to recovery of similarly faint discs in scattered light where the disc geometry is already known from spatially resolved continuum imaging. Deeper near-infrared or optical images are required to spatially resolve the scattered light disc, in particular to determine the degree of asymmetry in the dust scattering.

3.4. *Constraints on the dust composition*

Using the mean surface brightness from the scattered light detections we can use the inferred albedoes to constrain the dust grain composition. We calculate the scattering albedo $\omega = F_{\rm scat}/(F_{\rm scat} + F_{\rm therm})$, where $F_{\rm scat}$ is the scattered light fractional luminosity in the F160W filter, and $F_{\rm therm}$ is the dust continuum fractional luminosity. Following Choquet et al. (2018), we assume that the debris disc to be composed entirely of dust grains with a single size and of a single composition. It is further assumed that the same dust grains responsible for the scattered light are also responsible for the thermal emission so the value of $F_{\rm therm}$ is therefore held fixed for all the tested combinations of grain size and compositions, i.e. $L_{\rm dust}/L_\star = 2.6 \times 10^{-4}$. For consistency, we keep the dust mass of the disc fixed to that calculated for HD 105 based on its ALMA mm flux.

For each combination of grain size and composition we calculate the scattered light brightness of the disc at the observed orientation and inclination of HD 105, convolving the disc's scattered light SED with the F160W bandpass to determine the scattered light fractional brightness $F_{\rm scat}$, and hence the scattering albedo ω. The scattered light modelling is carried out using the 3-D radiative transfer code HYPERION (Robitaille 2011). We test grain sizes from 0.1 to 500 μm, and dust compositions of pure astronomical silicate, and water ice:astronomical silicate mixtures in the ratios 10:90, 30:70, and 50:50. Optical constants for the materials were taken from Draine (2003) (astronomical silicate) and Li & Greenberg (1998) (water ice). Calculation of the optical constants for composite materials was done using the Bruggeman effecive medium theory (Bruggeman 1935).

We find that dust grain sizes of a few microns, and either pure silicate or moderately icy compositions, are consistent with the dust albedo derived from the NICMOS-observed mean disc surface brightness.

3.5. *Revised SED model*

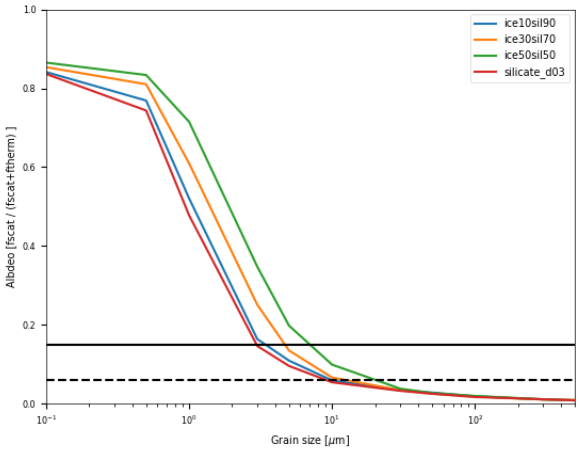

Figure 5. Plot of dust grain size vs. scattering albedo illustrating the constraints on dust grain size and composition possible with the new scattered light detection of HD 105's disc. The horizontal black lines denote the expected dust albedo required to reproduce the mean surface brightness from NICMOS (solid, $\omega = 0.15$) and SPHERE (dashed, $\omega = 0.06$). The coloured lines denote the scattering albedoes for discs composed of dust grains with a single size and composition. We find that silicate (or slightly icy) dust grains around a few μm in size are consistent with the NICMOS-derived scattering albedo; larger grains ($\geq$ 10 μm) are required to reproduce the SPHERE-derived albedo, but this would be inconsistent with the typical grain size of dust around Sun-like stars of a few to ten times the blow-out radius.

Here we combine the results previously determined from each dataset in order to model the full system. We use the disc architecture, as determined from the ALMA image, and the dust scattering albedo measurement from the scattered light images, as constraints in a radiative transfer model of the debris disc. We model the disc as being an annulus lying 70 to 100 au from the star with uniform radial surface brightness, as per the ALMA image. The disc is composed of compact, spherical dust grains described by a power law size distribution ($dn \propto a^{-q} da$) with exponent q spanning a size range from $a_{\rm min}$ to $a_{\rm max}$. The minimum dust grain size is a free parameter, but the maximum grain size is fixed at 10 mm to best replicate the millimetre wavelength photometry. The dust composition is assumed to be pure astronomical silicate (Draine 2003).

The resultant disc SED based on the best-fit model parameters is presented in Fig 6, and a summary of the best-fit disc properties (including the disc extent as fixed input) is provided in Table 4. The stellar photosphere component (dashed black line) is represented by a Castelli-Kurucz model (Castelli & Kurucz 2004) of appropriate to the stellar spectral type ($\log g = 4.5$ cm/s^2, $T_{\rm eff} = 6000$ K, [Fe/H] = 0.02) scaled to the optical and near-infrared fluxes (green data points). Blue and red data points denote *Spitzer*/IRS and *Herschel*/PACS fluxes, respectively. Grey data points are the excess (i.e. total - star) fluxes for wavelengths $> 20\mu$m. The individual models comprising the model grid used fit the observations is represented by the set of solid light grey lines, with the best-fit disc model denoted by the dashed dark grey line. The total model of the system (star+disc) is denoted by the solid black line.

4. DISCUSSION

There is a growing body of work examining the resolved extent of debris discs as a function of their host stars' luminosities (e.g., Booth et al. 2013; Morales et al. 2013; Pawellek et al. 2014; Pawellek & Krivov 2015). Generally, the resolved extent of debris discs around lower luminosity stars are found

Table 4
Modelling results from power law fit to disc emission.

Parameter	Range	Values	Spacing	Value
Semi-major axis (au)		1	Fixed	85
Belt width (au)		1	Fixed	30
α	0.0	1	Fixed	0.0
$a_{\rm min}$ (μm)	0.5 – 20.5	41	Linear	$3.25^{+3.00}_{-1.00}$
$a_{\rm max}$ (μm)	10^4	1	Fixed	10^4
q	2.50 – 4.50	11	Linear	$3.55^{+0.30}_{-0.15}$
Composition	—	1	—	Astro. sil.

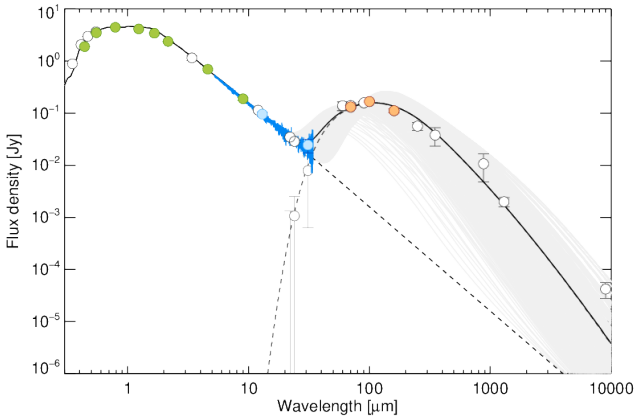

Figure 6. SED of HD 105, from power law modelling. Green dots denote optical and infrared photometry used to scale the stellar photosphere model. Blue lines and dots denote *Spitzer*/IRS data. Orange dots denote *Herschel*/PACS data. White dots denote ancilliary photometry from various literature sources (see Table 1). Uncertainties are 1σ. Dark grey data points denote excess values. The greyed-out region denotes the envelope of disc models produced from the grid parameter space. The dashed line denotes the individual stellar photosphere and disc components, whilst the solid line is the total emission.

to be greater than would be predicted from their blackbody temperature when compared to debris discs around higher luminosity stars.

We calculate the parameter Γ ($R_{\rm disc}/R_{\rm bb}$) for HD 105's disc using the relationship between stellar luminosity and disc temperature (radius) derived in Pawellek & Krivov (2015), tacitly assuming a dust composition of ice and astronomical silicate. We find $\Gamma = 2.43 \pm 0.42$, whereas a value of 4.94 ± 0.42 would have been predicted from the relationship shown in Pawellek & Krivov (2015). The dust grains that constitute the disc would thus be larger than we expect from Pawellek & Krivov (2015).

However, the minimum grain size inferred from our revised SED model is $3.25^{+3.00}_{-1.00}$ μm, consistent with the expectations of Pawellek & Krivov (2015). We also infer a size distribution exponent of $q = 3.55^{+0.30}_{-0.15}$. Our fit to the SED in the sub-millimetre is dominated by the far-infrared photometry, particularly the PACS 160 μm. In combination, the best-fit grain size and slopes parameters result in a steeper millimetre SED than inferred from the 9-mm ATCA data point. A relatively bright point source resides at 10″ from HD 105 in the ALMA image. Whilst this could be responsible for contaminating the APEX/LABOCA 880 μm data point, the ATCA beam was 5×4″, so it would be well separated from the disc at 9 mm. Alternatively, stellar chromospheric emission could be con-

tributing to the 9-mm flux measurement; enhanced emission (above that predicted from Rayleigh-Jean extrapolation) has been observed at millimetre wavelengths for several stars (e.g. MacGregor et al. 2013; Liseau et al. 2015; Chavez-Dagostino et al. 2016). We might also infer that the dust grains have enhanced emissivity at sub-millimetre wavelengths, an inference supported by the relatively shallow millimetre spectral slope index $\beta = 0.3$. Increasing the emissivity of dust grains at millimetre wavelengths can be achieved in many ways, including increasing the porosity or adopting a core-mantle model.

As an additional data point in the menagerie of resolved debris discs around Sun-like stars, we can examine the properties of the system in contrast to discs around stars of similar spectral type. The Jena catalogue of resolved debris discs[10] has 16 debris disc host stars that fit this criterion, taken from various literature sources (Krist et al. 2010; Ertel et al. 2011; Krist et al. 2012; Eiroa et al. 2013; Marshall et al. 2014b; Soummer et al. 2014; Kennedy et al. 2015; Dodson-Robinson et al. 2016; Choquet et al. 2016; Lieman-Sifry et al. 2016; Moór et al. 2016; Morales et al. 2016). Amongst this cohort, the properties of HD 105's disc are fairly typical, having a radius of $\sim$ 90 au (70 to 150 au), a typical dust temperature around 50 K (44 to 112 K), and a fractional luminosity of a few $\times 10^{-4}$ (1×10^{-5} to 5×10^{-3}). However, the constituents of this data set are heterogeneous, the discs having been resolved through various methods (optical, far-infrared, and millimetre) and the host stars having a wide variety of ages.

Through angular averaging we have managed to obtain a detection of the disc in scattered light. The angular averaging method, used here for the first time, facilitated a detection of disc scattered light and a deeper probe of the dust albedo than obtainable from standard analysis of the imaging observations through injection of a disc model; application of the angular averaging method to similar cases of continuum bright discs that remain undetected in scattered light are expected to yield further detections. The architecture of HD 105's disc bears striking resemblance to those of both HD 207129 (Krist et al. 2010; Marshall et al. 2011; Löhne et al. 2012) and HD 377 (Steele et al. 2016; Choquet et al. 2016). The albedo determined from the scattered light brightness calculated here is comparable to that found for dust grains in imaged discs of comparable fractional luminosity around nominally similar stars e.g. HD 207129 (albedo $\sim$ 0.05 Krist et al. 2010), and the properties of planetesimals in the Solar system.

5. CONCLUSIONS

We have presented an analysis combining the interpretation of high resolution stellar spectra alongside new and archival scattered light, far-infrared, and (sub-)millimetre imaging observations of HD 105 and its circumstellar disc. In combination, these observations have provided the basis for a more detailed interpretation of the system, including its architecture and evolutionary state.

From a Bayesian approach applied to stellar evolution models we confirm its youth, with an age of 50 ± 16 Myr. Additionally, we found activity indicators which are consistent with being at a pre-main sequence evolutionary stage. The disc's planetesimal belt is spatially resolved at millimetre wavelengths. The best-fitting architecture is found to be a single annulus with a semi-major axis of 85 au and a width of 30 au at a moderate inclination of 50°. The disc is more compact than would be predicted from application of simple stellar luminosity-disc radius relationships, suggesting that the dust grains comprising the disc are either large, or efficient emitters at (sub-)millimetre wavelengths (e.g. through increased porosity del Burgo et al. 2003).

There is no evidence of any offset between the planetesimal belt and the stellar position or any evidence of non-axisymmetric structure in the disc, either of which might imply the presence of a low mass companion interacting with the disc. No evidence of significant CO 2-1 line emission was found from the area of the disc, consistent with recent discoveries of gas in young (< 60 Myr) debris discs being found in discs around A-type stars.

Using an angular averaging technique to measure the scattered light radial profile, we have obtained a first detection of HD 105's debris disc in scattered light, determining a value for the dust albedo between 0.15 and 0.06. The application of this new technique to similar extant data sets, where the spatial extent of the disc is known from continuum emission but scattered light imaging has proven fruitless, should easily yield additional detections of debris discs in scattered light. This will provide an expanded pool of systems from which inferences can be drawn regarding their scattered light and thermal emission properties.

Comparison of the dust albedo inferred from the scattered light with simple grain models and simplifying assumptions with water ice/astronomical silicate compositions allows us to infer that the dust grains are consistent with either pure astronomical silicate such as is typically assumed for debris dust, or a moderately icy composition as might be expected for material lying well beyond the snow-line of the system and consistent with SED modelling of a number of other debris discs.

We thank the anonymous referee for their constructive criticism that improved the manuscript.

Herschel is an ESA space observatory with science instruments provided by European-led Principal Investigator consortia and with important participation from NASA.

This paper makes use of the following ALMA data: ADS/JAO.ALMA#2012.1.00437.S. ALMA is a partnership of ESO (representing its member states), NSF (USA) and NINS (Japan), together with NRC (Canada) and NSC and ASIAA (Taiwan) and KASI (Republic of Korea), in cooperation with the Republic of Chile. The Joint ALMA Observatory is operated by ESO, AUI/NRAO and NAOJ.

This research has made use of the SIMBAD database, operated at CDS, Strasbourg, France.

This research has made use of NASA's Astrophysics Data System.

This paper has made use of the Python packages ASTROPY (Astropy Collaboration et al. 2013, 2018), SCIPY (Jones et al. 2001–), MATPLOTLIB (Hunter 2007), and HYPERION (Robitaille 2011).

JPM acknowledges research support by the Ministry of Science and Technology of Taiwan under grants MOST104-2628-M-001-004-MY3 and MOST107-2119-M-001-031-MY3, and Academia Sinica under grant AS-IA-106-M03.

EC acknowledges support from NASA through Hubble Fellowship grant HF2-51355 awarded by STScI, which is operated by AURA, Inc. for NASA under contract NAS5-

[10] http://www.astro.uni-jena.de/index.php/theory/catalog-of-resolved-debris-disks.html

26555, for research carried out at the Jet Propulsion Laboratory, California Institute of Technology. This work is based on data reprocessed as part of the ALICE program, which was supported by NASA through grants HST-AR-12652 (PI: R. Soummer), HST-GO-11136 (PI: D. Golimowski), HST-GO-13855 (PI: E. Choquet), HST-GO-13331 (PI: L. Pueyo), and STScI Director's Discretionary Research funds.

CdB acknowledges that this work has been supported by Mexican CONACyT research grant CB-2012-183007

GMK is supported by the Royal Society as a Royal Society University Research Fellow.

LM acknowledges support from the Smithsonian Institution as a Submillimeter Array (SMA) Fellow.

REFERENCES

Allard, F., Homeier, D., & Freytag, B. 2012, Philosophical Transactions of the Royal Society of London Series A, 370, 2765
Astropy Collaboration, Robitaille, T. P., Tollerud, E. J., et al. 2013, A&A, 558, A33
Astropy Collaboration, Price-Whelan, A. M., Sipőcz, B. M., et al. 2018, AJ, 156, 123
Balog, Z., Müller, T., Nielbock, M., et al. 2014, Experimental Astronomy, 37, 129
Beckwith, S. V. W., Sargent, A. I., Chini, R. S., & Guesten, R. 1990, AJ, 99, 924
Beichman, C. A., Tanner, A., Bryden, G., et al. 2006, ApJ, 639, 1166
Beuzit, J.-L., Feldt, M., Dohlen, K., et al. 2008, in Society of Photo-Optical Instrumentation Engineers (SPIE) Conference Series, Vol. 7014, Society of Photo-Optical Instrumentation Engineers (SPIE) Conference Series
Booth, M., Kennedy, G., Sibthorpe, B., et al. 2013, MNRAS, 428, 1263
Bressan, A., Marigo, P., Girardi, L., et al. 2012, MNRAS, 427, 127
Bruggeman, D. A. G. 1935, Annalen der Physik, 416, 636
Buenzli, E., Thalmann, C., Vigan, A., et al. 2010, A&A, 524, L1
Carpenter, J. M., Bouwman, J., Mamajek, E. E., et al. 2009, ApJS, 181, 197
Castelli, F., & Kurucz, R. L. 2004, ArXiv Astrophysics e-prints, astro-ph/0405087
Chavez-Dagostino, M., Bertone, E., Cruz-Saenz de Miera, F., et al. 2016, MNRAS, 462, 2285
Chen, C. H., Sargent, B. A., Bohac, C., et al. 2006, ApJS, 166, 351
Chen, Y., Bressan, A., Girardi, L., et al. 2015, MNRAS, 452, 1068
Chen, Y., Girardi, L., Bressan, A., et al. 2014, MNRAS, 444, 2525
Choquet, É., Pueyo, L., Hagan, J. B., et al. 2014, in Proc. SPIE, Vol. 9143, Space Telescopes and Instrumentation 2014: Optical, Infrared, and Millimeter Wave, 914357
Choquet, É., Perrin, M. D., Chen, C. H., et al. 2016, ApJ, 817, L2
Choquet, É., Milli, J., Wahhaj, Z., et al. 2017, ApJ, 834, L12
Choquet, É., Bryden, G., Perrin, M. D., et al. 2018, ApJ, 854, 53
Coughlin, J. L., Mullally, F., Thompson, S. E., et al. 2016, ApJS, 224, 12
Cutri, R. M., Skrutskie, M. F., van Dyk, S., et al. 2003, VizieR Online Data Catalog, 2246
Debes, J. H., Weinberger, A. J., & Song, I. 2008, ApJ, 684, L41
Debes, J. H., Ygouf, M., Choquet, E., et al. 2016, Journal of Astronomical Telescopes, Instruments, and Systems, 2, 011010
del Burgo, C., & Allende Prieto, C. 2016, MNRAS, 463, 1400
—. 2018, MNRAS, 479, 1953
del Burgo, C., Héraudeau, P., & Ábrahám, P. 2003, in ESA Special Publication, Vol. 511, Exploiting the ISO Data Archive. Infrared Astronomy in the Internet Age, ed. C. Gry, S. Peschke, J. Matagne, P. Garcia-Lario, R. Lorente, & A. Salama, 339
del Burgo, C., Martín, E. L., Zapatero Osorio, M. R., & Hauschildt, P. H. 2009, A&A, 501, 1059
Dodson-Robinson, S. E., Su, K. Y. L., Bryden, G., Harvey, P., & Green, J. D. 2016, ApJ, 833, 183
Dohlen, K., Langlois, M., Saisse, M., et al. 2008, in Society of Photo-Optical Instrumentation Engineers (SPIE) Conference Series, Vol. 7014, Society of Photo-Optical Instrumentation Engineers (SPIE) Conference Series
Donaldson, J. K., Roberge, A., Chen, C. H., et al. 2012, ApJ, 753, 147
Draine, B. T. 2003, ApJ, 598, 1017
—. 2006, ApJ, 636, 1114
Eiroa, C., Marshall, J. P., Mora, A., et al. 2013, A&A, 555, A11
Ertel, S., Wolf, S., Metchev, S., et al. 2011, A&A, 533, A132
Ertel, S., Marshall, J. P., Augereau, J.-C., et al. 2014, A&A, 561, A114
Evans, D. W., Riello, M., De Angeli, F., et al. 2018, A&A, 616, A4
Foreman-Mackey, D., Morton, T. D., Hogg, D. W., Agol, E., & Schölkopf, B. 2016, AJ, 152, 206
Gaia Collaboration, Brown, A. G. A., Vallenari, A., et al. 2018, ArXiv e-prints, arXiv:1804.09365
Gaia Collaboration, Prusti, T., de Bruijne, J. H. J., et al. 2016, A&A, 595, A1
Gerard, B. L., & Marois, C. 2016, in Proc. SPIE, Vol. 9909, Adaptive Optics Systems V, 990958
Graham, J. R., Kalas, P. G., & Matthews, B. C. 2007, ApJ, 654, 595
Gray, D. F. 1992, The observation and analysis of stellar photospheres.
Greaves, J. S., Holland, W. S., Matthews, B. C., et al. 2016, MNRAS, 461, 3910
Hagan, J. B., Choquet, É., Soummer, R., & Vigan, A. 2018, AJ, 155, 179
Hedman, M. M., & Stark, C. C. 2015, ApJ, 811, 67
Hengst, S., Marshall, J. P., Horner, J., & Marsden, S. C. 2017, MNRAS, 468, 4725
Héraudeau, P., del Burgo, C., Stickel, M., et al. 2003, in ESA Special Publication, Vol. 511, Exploiting the ISO Data Archive. Infrared Astronomy in the Internet Age, ed. C. Gry, S. Peschke, J. Matagne, P. Garcia-Lario, R. Lorente, & A. Salama, 325
Hillenbrand, L. A., Carpenter, J. M., Kim, J. S., et al. 2008, ApJ, 677, 630
Hines, D. C., Schneider, G., Hollenbach, D., et al. 2007, ApJ, 671, L165
Holland, W. S., Matthews, B. C., Kennedy, G. M., et al. 2017, MNRAS, 470, 3606
Hughes, A. M., DuchÃªne, G., & Matthews, B. C. 2018, Annual Review of Astronomy and Astrophysics, 56, 541
Hunter, J. D. 2007, Computing in Science and Engineering, 9, 90
Ishihara, D., Onaka, T., Kataza, H., et al. 2010, A&A, 514, A1
Johnson, B. C., Lisse, C. M., Chen, C. H., et al. 2012, ApJ, 761, 45
Jones, E., Oliphant, T., Peterson, P., et al. 2001–, SciPy: Open source scientific tools for Python, [Online; accessed <today>]
Kennedy, G. M., Matrà, L., Marmier, M., et al. 2015, MNRAS, 449, 3121
Kral, Q., Matrà, L., Wyatt, M. C., & Kennedy, G. M. 2017, MNRAS, 469, 521
Krist, J. E., Stapelfeldt, K. R., Bryden, G., & Plavchan, P. 2012, AJ, 144, 45
Krist, J. E., Stapelfeldt, K. R., Bryden, G., et al. 2010, AJ, 140, 1051
Lafrenière, D., Marois, C., Doyon, R., & Barman, T. 2009, ApJ, 694, L148
Lawler, S. M., Beichman, C. A., Bryden, G., et al. 2009, ApJ, 705, 89
Lebouteiller, V., Barry, D. J., Spoon, H. W. W., et al. 2011, ApJS, 196, 8
Lebreton, J., Augereau, J.-C., Thi, W.-F., et al. 2012, A&A, 539, A17
Li, A., & Greenberg, J. M. 1998, A&A, 331, 291
Lieman-Sifry, J., Hughes, A. M., Carpenter, J. M., et al. 2016, ApJ, 828, 25
Lindegren, L., Lammers, U., Bastian, U., et al. 2016, A&A, 595, A4
Liseau, R., Eiroa, C., Fedele, D., et al. 2010, A&A, 518, L132
Liseau, R., Vlemmings, W., Bayo, A., et al. 2015, A&A, 573, L4
Löhne, T., Augereau, J.-C., Ertel, S., et al. 2012, A&A, 537, A110
Lowrance, P. J., McCarthy, C., Becklin, E. E., et al. 1999, ApJ, 512, L69
Lowrance, P. J., Becklin, E. E., Schneider, G., et al. 2005, AJ, 130, 1845
MacGregor, M. A., Wilner, D. J., Andrews, S. M., & Hughes, A. M. 2015, ApJ, 801, 59
MacGregor, M. A., Wilner, D. J., Rosenfeld, K. A., et al. 2013, ApJ, 762, L21
Maíz Apellániz, J. 2006, AJ, 131, 1184
Maness, H. L., Kalas, P., Peek, K. M. G., et al. 2009, ApJ, 707, 1098
Marino, S., Matrà, L., Stark, C., et al. 2016, MNRAS, 460, 2933
Marino, S., Wyatt, M. C., Panić, O., et al. 2017, MNRAS, 465, 2595
Marino, S., Carpenter, J., Wyatt, M. C., et al. 2018, MNRAS, 479, 5423
Marois, C., Lafrenière, D., Doyon, R., Macintosh, B., & Nadeau, D. 2006, ApJ, 641, 556
Marshall, J. P., Booth, M., Holland, W., et al. 2016, MNRAS, 459, 2893
Marshall, J. P., Maddison, S. T., Thilliez, E., et al. 2017, MNRAS, 468, 2719
Marshall, J. P., Löhne, T., Montesinos, B., et al. 2011, A&A, 529, A117
Marshall, J. P., Moro-Martín, A., Eiroa, C., et al. 2014a, A&A, 565, A15
Marshall, J. P., Kirchschlager, F., Ertel, S., et al. 2014b, A&A, 570, A114
Matrà, L., Marino, S., Kennedy, G. M., et al. 2018a, ApJ, 859, 72
Matrà, L., Panić, O., Wyatt, M. C., & Dent, W. R. F. 2015, MNRAS, 447, 3936
Matrà, L., Wilner, D. J., Öberg, K. I., et al. 2018b, ApJ, 853, 147
Matrà, L., MacGregor, M. A., Kalas, P., et al. 2017, ApJ, 842, 9
Matthews, B. C., Krivov, A. V., Wyatt, M. C., Bryden, G., & Eiroa, C. 2014, Protostars and Planets VI, 521
Mermilliod, J. C., Mermilliod, M., & Hauck, B. 1997, Astronomy and Astrophysics Supplement Series, 124, 349
Meshkat, T., Mawet, D., Bryan, M., et al. 2017, ArXiv e-prints, arXiv:1710.04185
Milli, J., Matrà, L., Mouillet, D.and Lagrange, A., et al. in prep., A&A
Milli, J., Mouillet, D., Lagrange, A.-M., et al. 2012, A&A, 545, A111
Milli, J., Hibon, P., Christiaens, V., et al. 2017a, A&A, 597, L2

Milli, J., Vigan, A., Mouillet, D., et al. 2017b, A&A, 599, A108
Mittal, T., Chen, C. H., Jang-Condell, H., et al. 2015, ApJ, 798, 87
Montesinos, B., Eiroa, C., Krivov, A. V., et al. 2016, ArXiv e-prints, arXiv:1605.05837
Moór, A., Kóspál, Á., Ábrahám, P., et al. 2016, ApJ, 826, 123
Moór, A., Curé, M., Kóspál, Á., et al. 2017, ArXiv e-prints, arXiv:1709.08414
Morales, F. Y., Bryden, G., Werner, M. W., & Stapelfeldt, K. R. 2013, ApJ, 776, 111
—. 2016, ApJ, 831, 97
Moro-Martín, A., Marshall, J. P., Kennedy, G., et al. 2015, ApJ, 801, 143
Nilsson, R., Liseau, R., Brandeker, A., et al. 2010, A&A, 518, A40
Olofsson, J., Samland, M., Avenhaus, H., et al. 2016, A&A, 591, A108
Ott, S. 2010, in Astronomical Society of the Pacific Conference Series, Vol. 434, Astronomical Data Analysis Software and Systems XIX, ed. Y. Mizumoto, K.-I. Morita, & M. Ohishi, 139
Panić, O., Holland, W. S., Wyatt, M. C., et al. 2013, MNRAS, 435, 1037
Paunzen, E. 2015, A&A, 580, A23
Pavlov, A., Feldt, M., & Henning, T. 2008, in Astronomical Society of the Pacific Conference Series, Vol. 394, Astronomical Data Analysis Software and Systems XVII, ed. R. W. Argyle, P. S. Bunclark, & J. R. Lewis, 581
Pawellek, N., & Krivov, A. V. 2015, MNRAS, 454, 3207
Pawellek, N., Krivov, A. V., Marshall, J. P., et al. 2014, ApJ, 792, 65
Perryman, M. A. C., Lindegren, L., Kovalevsky, J., et al. 1997, A&A, 323, L49
Pollack, J. B., Hollenbach, D., Beckwith, S., et al. 1994, ApJ, 421, 615
Pueyo, L. 2016, ApJ, 824, 117
Ricci, L., Carpenter, J. M., Fu, B., et al. 2015, ApJ, 798, 124
Robitaille, T. P. 2011, A&A, 536, A79
Rodigas, T. J., Hinz, P. M., Leisenring, J., et al. 2012, ApJ, 752, 57
Rodigas, T. J., Debes, J. H., Hinz, P. M., et al. 2014, ApJ, 783, 21
Schneider, G., Smith, B. A., Becklin, E. E., et al. 1999, ApJ, 513, L127
Schneider, G., Grady, C. A., Hines, D. C., et al. 2014, AJ, 148, 59
Schneider, G., Grady, C. A., Stark, C. C., et al. 2016, AJ, 152, 64
Schüppler, C., Krivov, A. V., Löhne, T., et al. 2016, MNRAS, 461, 2146
Schüppler, C., Löhne, T., Krivov, A. V., et al. 2014, A&A, 567, A127
Soummer, R., Pueyo, L., & Larkin, J. 2012, ApJ, 755, L28
Soummer, R., Sivaramakrishnan, A., Pueyo, L., Macintosh, B., & Oppenheimer, B. R. 2011, ApJ, 729, 144
Soummer, R., Perrin, M. D., Pueyo, L., et al. 2014, ApJ, 786, L23
Spangler, C., Sargent, A. I., Silverstone, M. D., Becklin, E. E., & Zuckerman, B. 2001, ApJ, 555, 932
Steele, A., Hughes, A. M., Carpenter, J., et al. 2016, ApJ, 816, 27
Tang, J., Bressan, A., Rosenfield, P., et al. 2014, MNRAS, 445, 4287
Thureau, N. D., Greaves, J. S., Matthews, B. C., et al. 2014, MNRAS, 445, 2558
Torres, C. A. O., da Silva, L., Quast, G. R., de la Reza, R., & Jilinski, E. 2000, AJ, 120, 1410
Tsantaki, M., Sousa, S. G., Santos, N. C., et al. 2014, A&A, 570, A80
Valenti, J. A., & Fischer, D. A. 2005, ApJS, 159, 141
van Leeuwen, F. 2007, A&A, 474, 653
Wahhaj, Z., Milli, J., Kennedy, G., et al. 2016, A&A, 596, L4
Weinberger, A. J., Becklin, E. E., Schneider, G., et al. 1999, ApJ, 525, L53
Wright, E. L., Eisenhardt, P. R. M., Mainzer, A. K., et al. 2010, AJ, 140, 1868
Wyatt, M. C., Kennedy, G., Sibthorpe, B., et al. 2012, MNRAS, 424, 1206
Zuckerman, B., & Becklin, E. E. 1993, ApJ, 414, 793
Zuckerman, B., & Webb, R. A. 2000, ApJ, 535, 959